Vol. 3(Iss. 1) 2026, pp.238-256, African Scientific Annual Review www.asarev.net ISSN: 3007-0902

Three-dimensional navier–stokes formulation, finite element discretization, stability analysis, and validation for crude oil pipeline flow

Sarah Khaindi Wandabwa[1*]
David Angwenyi[2]
Frankline Tireito[3]

[1,2,3]Department of Mathematics, Masinde Muliro University of Science and Technology, Kakamega, Kenya

[1*]sarahwandabwa2023@gmail.com

https://doi.org/10.51867/asarev.maths.3.1.21

Abstract

This paper presents a comprehensive formulation of the three-dimensional Navier–Stokes equations for viscous, incompressible crude oil flow in pipelines, its finite element discretization, energy stability analysis, and thorough validation. The governing equations are derived from first principles using the Reynolds transport theorem. A Newtonian constitutive relation appropriate for light to medium crude oils is adopted. The weak formulation is obtained via the Galerkin method, and the finite element discretization employs Taylor–Hood P_2–P_1 elements that satisfy the discrete inf–sup condition. The Crank–Nicolson scheme is implemented for temporal integration. For turbulent flows, the standard k-ϵ model is incorporated. Energy stability is proved for both continuous and semidiscrete formulations. The model is validated against the analytical Hagen–Poiseuille solution for laminar flow, achieving maximum relative errors below 0.05% and a root mean square error of 8.2×10^{-5} m/s. For turbulent flow, validation against Laufer's experimental data at $Re = 50,000$ yields a coefficient of determination $R^2 = 0.996$ and errors less than 4% for wall shear stress and skin friction coefficient. A detailed implementation section is included, covering mesh generation, solver specifics, and computational costs. These results confirm the model's accuracy and reliability for predicting velocity profiles, pressure drops, and turbulence characteristics in pipeline flows.

MSC2010 Subject Classification: 65N30, 76D05, 76F60, 35Q30
Keywords: Navier–Stokes equations, finite element method, crude oil pipeline, Taylor–Hood elements, energy stability, k-ϵ turbulence model.

1 Introduction

The transportation of crude oil through long-distance pipelines is a critical component of global energy infrastructure. Accurate prediction of flow behavior, pressure drop, and energy requirements is essential for safe and economic pipeline design. The Navier–Stokes equations provide the most

complete mathematical description of viscous fluid motion, capturing both laminar and turbulent regimes. However, their non-linear and coupled nature makes analytical solutions possible only for highly simplified geometries and conditions. The finite element method (FEM) has emerged as a powerful numerical tool for solving these equations over complex three-dimensional domains, offering flexibility in mesh generation and boundary condition handling [1, 6].

Despite the widespread use of FEM in computational fluid dynamics, there remains a gap in systematic application to crude oil pipeline flows, particularly in addressing the full 3D Navier–Stokes equations with appropriate turbulence modeling and stability guarantees for African pipeline infrastructure. This paper addresses the objectives of the research: to formulate the 3D governing equations, develop a finite element model for pipeline systems, and conduct stability analysis and validation against analytical and experimental results. The formulation is derived from first principles, with careful attention to the physical assumptions and mathematical structure. The finite element discretization is detailed, including the choice of element pairs, temporal integration, and turbulence closure. Energy stability is rigorously proved, and the model is validated against benchmark solutions and experimental data.

The significance of this work extends beyond academic interest. In the petroleum industry, major infrastructure projects such as the Turkana crude oil project and the proposed Lamu-Port-South Sudan-Ethiopia Transport (LAPSSET) corridor depend on long-distance pipeline networks to transport crude oil from production fields to export terminals. The ability to accurately simulate flow behavior in these pipelines is essential for optimizing energy consumption, ensuring safety, and reducing operational costs. Traditional analytical solutions are limited to simple cases such as steady, smooth flow in straight round pipes and therefore do not work well for real-world conditions involving turbulence, irregular geometries, and varying fluid properties [2, 15].

This research addresses the gap by developing and testing a 3D FEM model that improves on older methods by giving more accurate and flexible simulations of crude oil flow. The model is intended to make oil transport safer, more reliable, and cheaper, thereby contributing to better mathematical and engineering design. Section 2 presents the mathematical preliminaries and function spaces. Section 3 derives the conservation of mass and momentum equations. Section 4 discusses boundary conditions and the dimensionless form of the equations. Section 5 presents the finite element discretization, including the weak formulation, Taylor–Hood elements, temporal discretization, and turbulence modeling. Section 6 provides the energy stability analysis for both continuous and semidiscrete formulations. Section 7 discusses implementation and solution algorithms. Section 8 presents mesh convergence results. Section 9 validates the model against Hagen–Poiseuille flow and Laufer's experimental data. Section 10 discusses the results and model limitations, and Section 11 concludes the paper.

2 Mathematical Preliminaries

Before deriving the Navier–Stokes equations, we establish the mathematical framework. Let $\Omega \subset \mathbb{R}^3$ be a bounded, connected, open set with Lipschitz boundary Γ. The function spaces used throughout are defined as follows.

Definition 1. The Lebesgue space $L^2(\Omega)$ consists of all measurable functions f such that $\|f\|_{L^2(\Omega)} = \left(\int_\Omega |f|^2 d\Omega\right)^{1/2} < \infty$.
Definition 2. The Sobolev space $H^1(\Omega) = \{f \in L^2(\Omega) : \nabla f \in [L^2(\Omega)]^3\}$ with norm $\|f\|^2_{H^1(\Omega)} = \|f\|^2_{L^2} + \|\nabla f\|^2_{L^2}$.

For vector-valued functions, $\mathbf{H}^1(\Omega) = [H^1(\Omega)]^3$ and $\mathbf{L}^2(\Omega) = [L^2(\Omega)]^3$.

Two essential theorems are repeatedly used.
Theorem 3 (Divergence Theorem)**.** *For a vector field* $\mathbf{F} \in \mathbf{H}^1(\Omega)$*,*

$$\int_\Omega \nabla \cdot \mathbf{F}\, d\Omega = \int_\Gamma \mathbf{F} \cdot \mathbf{n}\, d\Gamma. \tag{1}$$

Theorem 4 (Reynolds Transport Theorem)**.** *For a material volume* $V(t)$ *moving with the fluid,*

$$\frac{d}{dt}\int_{V(t)} f(\mathbf{x}, t)\, dV = \int_{V(t)} \frac{\partial f}{\partial t}\, dV + \int_{\partial V(t)} f\, \mathbf{u} \cdot \mathbf{n}\, dS. \tag{2}$$

These theorems are the cornerstones for deriving conservation laws.

3 Conservation of Mass

The principle of mass conservation states that mass can neither be created nor destroyed. For a fixed control volume V, the rate of change of mass inside equals the net mass flux through the boundary.
Theorem 5. *For any fixed control volume* $V \subset \Omega$*,*

$$\frac{d}{dt}\int_V \rho\, dV = -\int_{\partial V} \rho\, \mathbf{u} \cdot \mathbf{n}\, dS. \tag{3}$$

Proof. Consider a material volume $V(t)$ that always contains the same fluid particles. Since mass is conserved for a material volume, the total mass within $V(t)$ remains constant:

$$\frac{d}{dt}\int_{V(t)} \rho\, dV = 0. \tag{4}$$

Using the Reynolds transport theorem with $f = \rho$ gives:

$$\frac{d}{dt}\int_{V(t)} \rho\, dV = \int_{V(t)} \frac{\partial \rho}{\partial t}\, dV + \int_{\partial V(t)} \rho \mathbf{u} \cdot \mathbf{n}\, dS. \tag{5}$$

Combining (4) and (5) yields:

$$\int_{V(t)} \frac{\partial \rho}{\partial t}\, dV + \int_{\partial V(t)} \rho \mathbf{u} \cdot \mathbf{n}\, dS = 0. \tag{6}$$

At time t, the material volume coincides with a fixed control volume V, so $V(t) = V$ and $\partial V(t) = \partial V$. Thus:

$$\int_V \frac{\partial \rho}{\partial t}\, dV + \int_{\partial V} \rho \mathbf{u} \cdot \mathbf{n}\, dS = 0. \tag{7}$$

Rearranging (7) gives the integral form:

$$\frac{d}{dt} \int_V \rho\, dV = -\int_{\partial V} \rho \mathbf{u} \cdot \mathbf{n}\, dS. \tag{8}$$

Applying the divergence theorem to the surface integral in (8):

$$\int_{\partial V} \rho \mathbf{u} \cdot \mathbf{n}\, dS = \int_V \nabla \cdot (\rho \mathbf{u})\, dV. \tag{9}$$

Substituting (9) into (8):

$$\int_V \frac{\partial \rho}{\partial t}\, dV + \int_V \nabla \cdot (\rho \mathbf{u})\, dV = 0. \tag{10}$$

Combining integrals over the same volume:

$$\int_V \left[\frac{\partial \rho}{\partial t} + \nabla \cdot (\rho \mathbf{u}) \right] dV = 0. \tag{11}$$

Since the control volume V is arbitrary and the integrand is continuous, the integrand must vanish at every point in Ω:

$$\frac{\partial \rho}{\partial t} + \nabla \cdot (\rho \mathbf{u}) = 0. \tag{12}$$

Under the assumption of incompressibility, the density ρ is constant in both space and time. Therefore $\partial \rho / \partial t = 0$ and $\nabla \rho = \mathbf{0}$. Substituting into (12) gives:

$$\nabla \cdot \mathbf{u} = 0. \tag{13}$$

In Cartesian coordinates (x, y, z) with velocity components (u, v, w), this expands to:

$$\frac{\partial u}{\partial x} + \frac{\partial v}{\partial y} + \frac{\partial w}{\partial z} = 0. \tag{14}$$

□

The incompressibility assumption is valid for crude oil because its compressibility is less than 1% under typical pipeline pressures (0.5–10 MPa) [2]. The bulk modulus of crude oil is approximately 1.5×10^9 Pa; a pressure change of 10 MPa yields a relative density change of about 0.67%, which is negligible for engineering calculations.

4 Conservation of Momentum

Newton's second law applied to a fluid element yields the momentum conservation equation. For a material volume $V(t)$:

$$\frac{d}{dt}\int_{V(t)} \rho\mathbf{u}\, dV = \int_{V(t)} \rho\mathbf{f}\, dV + \int_{\partial V(t)} \boldsymbol{\sigma}\cdot\mathbf{n}\, dS, \tag{15}$$

where $\mathbf{f}$ is the body force per unit mass (e.g., gravity $\mathbf{g}$) and $\boldsymbol{\sigma}$ is the Cauchy stress tensor.

Proof. Apply Newton's second law to a material volume. Using the Reynolds transport theorem for the left-hand side of (15):

$$\frac{d}{dt}\int_{V(t)} \rho\mathbf{u}\, dV = \int_{V(t)} \frac{\partial(\rho\mathbf{u})}{\partial t}\, dV + \int_{\partial V(t)} \rho\mathbf{u}(\mathbf{u}\cdot\mathbf{n})\, dS. \tag{16}$$

Substituting (16) into (15):

$$\int_{V(t)} \frac{\partial(\rho\mathbf{u})}{\partial t}\, dV + \int_{\partial V(t)} \rho\mathbf{u}(\mathbf{u}\cdot\mathbf{n})\, dS = \int_{V(t)} \rho\mathbf{f}\, dV + \int_{\partial V(t)} \boldsymbol{\sigma}\cdot\mathbf{n}\, dS. \tag{17}$$

At time t, the material volume coincides with a fixed control volume V:

$$\int_{V} \frac{\partial(\rho\mathbf{u})}{\partial t}\, dV + \int_{\partial V} \rho\mathbf{u}(\mathbf{u}\cdot\mathbf{n})\, dS = \int_{V} \rho\mathbf{f}\, dV + \int_{\partial V} \boldsymbol{\sigma}\cdot\mathbf{n}\, dS. \tag{18}$$

Rearranging (18) gives the integral form:

$$\frac{d}{dt}\int_{V} \rho\mathbf{u}\, dV = -\int_{\partial V} \rho\mathbf{u}(\mathbf{u}\cdot\mathbf{n})\, dS + \int_{V} \rho\mathbf{f}\, dV + \int_{\partial V} \boldsymbol{\sigma}\cdot\mathbf{n}\, dS. \tag{19}$$

Apply the divergence theorem to the surface integrals in (19). For the convective term:

$$\int_{\partial V} \rho\mathbf{u}(\mathbf{u}\cdot\mathbf{n})\, dS = \int_{V} \nabla\cdot(\rho\mathbf{u}\otimes\mathbf{u})\, dV. \tag{20}$$

For the stress term:

$$\int_{\partial V} \boldsymbol{\sigma}\cdot\mathbf{n}\, dS = \int_{V} \nabla\cdot\boldsymbol{\sigma}\, dV. \tag{21}$$

Substituting (20) and (21) into (19):

$$\int_{V} \frac{\partial(\rho\mathbf{u})}{\partial t}\, dV + \int_{V} \nabla\cdot(\rho\mathbf{u}\otimes\mathbf{u})\, dV = \int_{V} \rho\mathbf{f}\, dV + \int_{V} \nabla\cdot\boldsymbol{\sigma}\, dV. \tag{22}$$

Combining integrals:

$$\int_{V} \left[\frac{\partial(\rho\mathbf{u})}{\partial t} + \nabla\cdot(\rho\mathbf{u}\otimes\mathbf{u}) - \rho\mathbf{f} - \nabla\cdot\boldsymbol{\sigma}\right] dV = 0. \tag{23}$$

Since V is arbitrary, the integrand must vanish:

$$\frac{\partial(\rho \mathbf{u})}{\partial t} + \nabla \cdot (\rho \mathbf{u} \otimes \mathbf{u}) = \rho \mathbf{f} + \nabla \cdot \boldsymbol{\sigma}. \tag{24}$$

□

4.1 Constitutive Relation for Newtonian Fluids

The Cauchy stress tensor is decomposed into pressure and viscous parts:

$$\boldsymbol{\sigma} = -p\mathbf{I} + \boldsymbol{\tau}, \tag{25}$$

where p is the thermodynamic pressure and $\boldsymbol{\tau}$ is the deviatoric stress tensor. For a Newtonian fluid, the viscous stress is linearly proportional to the rate of strain:

$$\boldsymbol{\tau} = \lambda(\nabla \cdot \mathbf{u})\mathbf{I} + \mu \left(\nabla \mathbf{u} + (\nabla \mathbf{u})^T\right). \tag{26}$$

For incompressible flow, $\nabla \cdot \mathbf{u} = 0$, so the term involving λ vanishes, leaving:

$$\boldsymbol{\tau} = \mu \left(\nabla \mathbf{u} + (\nabla \mathbf{u})^T\right). \tag{27}$$

Substituting (25) and (27) into (24):

$$\frac{\partial(\rho \mathbf{u})}{\partial t} + \nabla \cdot (\rho \mathbf{u} \otimes \mathbf{u}) = \rho \mathbf{f} - \nabla p + \nabla \cdot \left[\mu \left(\nabla \mathbf{u} + (\nabla \mathbf{u})^T\right)\right]. \tag{28}$$

Assuming constant density ρ and dynamic viscosity μ:

$$\frac{\partial(\rho \mathbf{u})}{\partial t} = \rho \frac{\partial \mathbf{u}}{\partial t}, \tag{29}$$

$$\nabla \cdot (\rho \mathbf{u} \otimes \mathbf{u}) = \rho(\mathbf{u} \cdot \nabla)\mathbf{u} + \rho \mathbf{u}(\nabla \cdot \mathbf{u}) = \rho(\mathbf{u} \cdot \nabla)\mathbf{u}, \quad \text{since } \nabla \cdot \mathbf{u} = 0, \tag{30}$$

$$\nabla \cdot \left[\mu \left(\nabla \mathbf{u} + (\nabla \mathbf{u})^T\right)\right] = \mu \nabla^2 \mathbf{u} + \mu \nabla(\nabla \cdot \mathbf{u}) = \mu \nabla^2 \mathbf{u}. \tag{31}$$

Substituting (29), (30), and (31) into (28) yields the Navier–Stokes equations:

$$\rho \left(\frac{\partial \mathbf{u}}{\partial t} + (\mathbf{u} \cdot \nabla)\mathbf{u}\right) = -\nabla p + \mu \nabla^2 \mathbf{u} + \rho \mathbf{g}. \tag{32}$$

In component form:

$$\rho\left(\frac{\partial u}{\partial t}+u\frac{\partial u}{\partial x}+v\frac{\partial u}{\partial y}+w\frac{\partial u}{\partial z}\right)=-\frac{\partial p}{\partial x}+\mu\left(\frac{\partial^2 u}{\partial x^2}+\frac{\partial^2 u}{\partial y^2}+\frac{\partial^2 u}{\partial z^2}\right)+\rho g_x, \tag{33}$$

$$\rho\left(\frac{\partial v}{\partial t}+u\frac{\partial v}{\partial x}+v\frac{\partial v}{\partial y}+w\frac{\partial v}{\partial z}\right)=-\frac{\partial p}{\partial y}+\mu\left(\frac{\partial^2 v}{\partial x^2}+\frac{\partial^2 v}{\partial y^2}+\frac{\partial^2 v}{\partial z^2}\right)+\rho g_y, \tag{34}$$

$$\rho\left(\frac{\partial w}{\partial t}+u\frac{\partial w}{\partial x}+v\frac{\partial w}{\partial y}+w\frac{\partial w}{\partial z}\right)=-\frac{\partial p}{\partial z}+\mu\left(\frac{\partial^2 w}{\partial x^2}+\frac{\partial^2 w}{\partial y^2}+\frac{\partial^2 w}{\partial z^2}\right)+\rho g_z. \tag{35}$$

5 Boundary Conditions

To obtain a unique solution, appropriate boundary conditions must be specified. The following conditions are used. At the wall, the no-slip condition is imposed, requiring the velocity to be zero everywhere on the solid boundary. At the inlet, a prescribed velocity profile is specified; for laminar flow this is a parabolic profile given by $u_{\text{in}}(r) = 2U_{\text{avg}}(1 - r^2/R^2)$, while for turbulent flow a uniform or power-law profile may be used. At the outlet, a do-nothing (natural) condition is applied, which takes the form $\mu\partial\mathbf{u}/\partial n - p\mathbf{n} = \mathbf{0}$ and arises naturally from the weak formulation, allowing the flow to exit freely without spurious reflections. For the k-ϵ model, boundary conditions are $k = 0$ at the wall (for wall-resolved simulations) and ϵ computed from the wall function approach.

6 Dimensionless Form and Reynolds Number

Introduce characteristic scales: velocity U, length L (pipe diameter D), time L/U, and pressure ρU^2. Define dimensionless variables:

$$\mathbf{x}^* = \frac{\mathbf{x}}{L}, \quad t^* = \frac{tU}{L}, \quad \mathbf{u}^* = \frac{\mathbf{u}}{U}, \quad p^* = \frac{p}{\rho U^2}, \quad \nabla^* = L\nabla. \tag{36}$$

Substitute (36) into (32). The inertial term becomes:

$$\rho\left(\frac{\partial \mathbf{u}}{\partial t}+(\mathbf{u}\cdot\nabla)\mathbf{u}\right)=\frac{\rho U^2}{L}\left(\frac{\partial \mathbf{u}^*}{\partial t^*}+(\mathbf{u}^*\cdot\nabla^*)\mathbf{u}^*\right). \tag{37}$$

The pressure gradient term:

$$-\nabla p = -\frac{\rho U^2}{L}\nabla^* p^*. \tag{38}$$

The viscous term:

$$\mu\nabla^2\mathbf{u} = \frac{\mu U}{L^2}\nabla^{*2}\mathbf{u}^*. \tag{39}$$

The gravity term:

$$\rho\mathbf{g} = \frac{\rho U^2}{L}\frac{1}{Fr^2}\mathbf{g}^*, \tag{40}$$

where $Fr = U/\sqrt{gL}$ is the Froude number. Substituting (37)–(40) into (32) and multiplying by $L/(\rho U^2)$ gives the dimensionless Navier–Stokes equations:

$$\frac{\partial \mathbf{u}^*}{\partial t^*} + (\mathbf{u}^* \cdot \nabla^*)\mathbf{u}^* = -\nabla^* p^* + \frac{1}{Re}\nabla^{*2}\mathbf{u}^* + \frac{1}{Fr^2}\mathbf{g}^*, \tag{41}$$

where

$$Re = \frac{\rho U L}{\mu} = \frac{UL}{\nu}, \quad Fr = \frac{U}{\sqrt{gL}}. \tag{42}$$

For typical crude oil pipeline conditions: $\rho = 850$ kg/m^3, $\mu = 0.01$ Pa·s, $D = 0.5$ m, $U = 1.0$ m/s, we have:

$$Re = \frac{850 \times 1.0 \times 0.5}{0.01} = 42,500, \tag{43}$$

which is well above the critical value of 4,000, indicating turbulent flow. Hence turbulence modeling is required.

7 Finite Element Discretization

7.1 Weak Formulation

Define the velocity space $\mathbf{V} = \{\mathbf{v} \in \mathbf{H}^1(\Omega) : \mathbf{v} = \mathbf{0} \text{ on } \Gamma_{\text{wall}} \cup \Gamma_{\text{in}}\}$ and pressure space $Q = L^2(\Omega)/\mathbb{R}$ (quotient by constants). The weak formulation is: find $(\mathbf{u}, p) \in \mathbf{V} \times Q$ such that for all test functions $(\mathbf{v}, q) \in \mathbf{V} \times Q$,

$$\int_\Omega \rho \frac{\partial \mathbf{u}}{\partial t} \cdot \mathbf{v}\, d\Omega + \int_\Omega \rho(\mathbf{u} \cdot \nabla)\mathbf{u} \cdot \mathbf{v}\, d\Omega + \int_\Omega \mu \nabla \mathbf{u} : \nabla \mathbf{v}\, d\Omega - \int_\Omega p \nabla \cdot \mathbf{v}\, d\Omega = \int_\Omega \rho \mathbf{g} \cdot \mathbf{v}\, d\Omega, \tag{44}$$

$$\int_\Omega q \nabla \cdot \mathbf{u}\, d\Omega = 0. \tag{45}$$

The integration by parts transfers one derivative from the velocity to the test function, reducing the regularity requirement from $\mathbf{H}^2$ to $\mathbf{H}^1$, which is essential for finite element approximations [14, 11].

7.2 Taylor–Hood Elements

The computational domain is partitioned into tetrahedral elements. For each element, the velocity is approximated by quadratic (P_2) polynomials and pressure by linear (P_1) polynomials. The finite element spaces are:

$$\mathbf{V}_h = \{\mathbf{v}_h \in \mathbf{V} : \mathbf{v}_h|_K \in [P_2(K)]^3, \forall K \in \mathcal{T}_h\}, \quad Q_h = \{q_h \in Q : q_h|_K \in P_1(K), \forall K \in \mathcal{T}_h\}. \tag{46}$$

This element pair satisfies the discrete inf–sup (LBB) condition, ensuring stability and uniqueness of the pressure solution [3, 13]. The basis functions are defined locally: for velocity, there are 10 nodes

per tetrahedron (4 vertices + 6 edge midpoints); for pressure, 4 nodes (vertices). The global finite element expansions are:

$$\mathbf{u}_h(\mathbf{x},t) = \sum_{j=1}^{N_u} \mathbf{U}_j(t)\boldsymbol{\Phi}_j(\mathbf{x}), \quad p_h(\mathbf{x},t) = \sum_{k=1}^{N_p} P_k(t)\Psi_k(\mathbf{x}). \tag{47}$$

Substitution into the weak form yields the discrete system of ordinary differential equations:

$$\mathbf{M}\frac{d\mathbf{U}}{dt} + \mathbf{C}(\mathbf{U})\mathbf{U} + \mathbf{K}\mathbf{U} + \mathbf{B}^T\mathbf{P} = \mathbf{F}, \quad \mathbf{B}\mathbf{U} = \mathbf{0}, \tag{48}$$

where the discrete system involves several matrices: the mass matrix $\mathbf{M}_{ij} = \int_\Omega \rho\boldsymbol{\Phi}_i \cdot \boldsymbol{\Phi}_j \, d\Omega$, the convection matrix $\mathbf{C}_{ij}(\mathbf{U}) = \int_\Omega \rho(\mathbf{u}_h \cdot \nabla\boldsymbol{\Phi}_i) \cdot \boldsymbol{\Phi}_j \, d\Omega$ which is non-linear, the stiffness (diffusion) matrix $\mathbf{K}_{ij} = \int_\Omega \mu\nabla\boldsymbol{\Phi}_i : \nabla\boldsymbol{\Phi}_j \, d\Omega$, the divergence matrix $\mathbf{B}_{kj} = -\int_\Omega \Psi_k \nabla \cdot \boldsymbol{\Phi}_j \, d\Omega$, and the force vector $\mathbf{F}_i = \int_\Omega \rho\mathbf{g} \cdot \boldsymbol{\Phi}_i \, d\Omega$.

7.3 Temporal Discretization

The Crank–Nicolson scheme is employed for its second-order accuracy and unconditional stability for the diffusion part. The fully discrete system reads:

$$\mathbf{M}\frac{\mathbf{U}^{n+1} - \mathbf{U}^n}{\Delta t} + \mathbf{K}\frac{\mathbf{U}^{n+1} + \mathbf{U}^n}{2} + \frac{1}{2}\left[\mathbf{C}(\mathbf{U}^{n+1})\mathbf{U}^{n+1} + \mathbf{C}(\mathbf{U}^n)\mathbf{U}^n\right] + \mathbf{B}^T\frac{\mathbf{P}^{n+1} + \mathbf{P}^n}{2} = \frac{\mathbf{F}^{n+1} + \mathbf{F}^n}{2}, \tag{49}$$

$$\mathbf{B}\mathbf{U}^{n+1} = 0. \tag{50}$$

This is an implicit non-linear system that must be solved at each time step [4, 6].

7.4 Turbulence Modeling

For turbulent flows ($Re > 4000$), the standard k-ϵ model is used [7]. The Reynolds-averaged Navier–Stokes (RANS) equations are obtained by decomposing the velocity and pressure into mean and fluctuating parts. The turbulent stresses are modeled using the Boussinesq hypothesis:

$$-\rho\overline{\mathbf{u}'\mathbf{u}'} = \mu_t\left(\nabla\overline{\mathbf{u}} + (\nabla\overline{\mathbf{u}})^T\right) - \frac{2}{3}\rho k\mathbf{I}, \tag{51}$$

where $k = \frac{1}{2}\overline{\mathbf{u}' \cdot \mathbf{u}'}$ is turbulent kinetic energy and $\mu_t = \rho C_\mu k^2/\epsilon$ is the eddy viscosity, with ϵ the dissipation rate.

The transport equations for k and ϵ are:

$$\frac{\partial k}{\partial t} + (\mathbf{u} \cdot \nabla)k = \nabla \cdot \left[\left(\nu + \frac{\nu_t}{\sigma_k} \right) \nabla k \right] + P_k - \epsilon, \tag{52}$$

$$\frac{\partial \epsilon}{\partial t} + (\mathbf{u} \cdot \nabla)\epsilon = \nabla \cdot \left[\left(\nu + \frac{\nu_t}{\sigma_\epsilon} \right) \nabla \epsilon \right] + C_{1\epsilon} \frac{\epsilon}{k} P_k - C_{2\epsilon} \frac{\epsilon^2}{k}, \tag{53}$$

where $P_k = \mu_t \nabla \mathbf{u} : (\nabla \mathbf{u} + (\nabla \mathbf{u})^T)$ is the production of turbulent kinetic energy. The model constants are: $C_\mu = 0.09$, $C_{1\epsilon} = 1.44$, $C_{2\epsilon} = 1.92$, $\sigma_k = 1.0$, $\sigma_\epsilon = 1.3$. These equations are discretized using the same finite element framework. The choice of the standard k-ϵ model is justified for this study because it is the most widely validated turbulence model for pipe flows, has moderate computational cost compared to more complex models (RNG, SST), and provides sufficient engineering accuracy for the pressure drop predictions required in this work. However, its limitations for flows with separation and strong curvature are acknowledged and discussed in Section 10.

8 Energy Stability Analysis

8.1 Continuous Energy Estimate

Consider the Navier–Stokes equations with homogeneous Dirichlet boundary conditions ($\mathbf{u} = \mathbf{0}$ on Γ) and no body forces ($\mathbf{g} = 0$). Define the kinetic energy $E(t) = \frac{1}{2} \int_\Omega \rho |\mathbf{u}|^2 \, d\Omega$.

Theorem 6. *The kinetic energy satisfies:*

$$\frac{dE}{dt} = -\int_\Omega \mu |\nabla \mathbf{u}|^2 \, d\Omega \leq 0. \tag{54}$$

Thus, energy decreases monotonically due to viscous dissipation.

Proof. Multiply the momentum equation (32) (with $\mathbf{g} = 0$) by $\mathbf{u}$ and integrate over Ω:

$$\int_\Omega \rho \mathbf{u} \cdot \frac{\partial \mathbf{u}}{\partial t} \, d\Omega + \int_\Omega \rho \mathbf{u} \cdot (\mathbf{u} \cdot \nabla)\mathbf{u} \, d\Omega = -\int_\Omega \mathbf{u} \cdot \nabla p \, d\Omega + \int_\Omega \mu \mathbf{u} \cdot \nabla^2 \mathbf{u} \, d\Omega. \tag{55}$$

The first term on the left-hand side is:

$$\int_\Omega \rho \mathbf{u} \cdot \frac{\partial \mathbf{u}}{\partial t} \, d\Omega = \frac{1}{2} \frac{d}{dt} \int_\Omega \rho |\mathbf{u}|^2 \, d\Omega = \frac{dE}{dt}. \tag{56}$$

For the convective term, note that:

$$\mathbf{u} \cdot (\mathbf{u} \cdot \nabla)\mathbf{u} = \frac{1}{2} \mathbf{u} \cdot \nabla |\mathbf{u}|^2. \tag{57}$$

Thus:

$$\int_\Omega \rho \mathbf{u} \cdot (\mathbf{u} \cdot \nabla)\mathbf{u}\, d\Omega = \frac{1}{2} \int_\Omega \rho \mathbf{u} \cdot \nabla |\mathbf{u}|^2\, d\Omega. \tag{58}$$

Using the identity $\nabla \cdot (\rho |\mathbf{u}|^2 \mathbf{u}) = \rho \mathbf{u} \cdot \nabla |\mathbf{u}|^2 + \rho |\mathbf{u}|^2 \nabla \cdot \mathbf{u}$, and since $\nabla \cdot \mathbf{u} = 0$, we have:

$$\rho \mathbf{u} \cdot \nabla |\mathbf{u}|^2 = \nabla \cdot (\rho |\mathbf{u}|^2 \mathbf{u}). \tag{59}$$

Therefore:

$$\int_\Omega \rho \mathbf{u} \cdot (\mathbf{u} \cdot \nabla)\mathbf{u}\, d\Omega = \frac{1}{2} \int_\Omega \nabla \cdot (\rho |\mathbf{u}|^2 \mathbf{u})\, d\Omega = \frac{1}{2} \int_\Gamma \rho |\mathbf{u}|^2 \mathbf{u} \cdot \mathbf{n}\, d\Gamma. \tag{60}$$

Since $\mathbf{u} = \mathbf{0}$ on Γ (homogeneous Dirichlet), the boundary integral vanishes. Thus:

$$\int_\Omega \rho \mathbf{u} \cdot (\mathbf{u} \cdot \nabla)\mathbf{u}\, d\Omega = 0. \tag{61}$$

For the pressure term:

$$-\int_\Omega \mathbf{u} \cdot \nabla p\, d\Omega = -\int_\Omega \nabla \cdot (p\mathbf{u})\, d\Omega + \int_\Omega p \nabla \cdot \mathbf{u}\, d\Omega. \tag{62}$$

Using the divergence theorem and $\nabla \cdot \mathbf{u} = 0$:

$$-\int_\Omega \mathbf{u} \cdot \nabla p\, d\Omega = -\int_\Gamma p\mathbf{u} \cdot \mathbf{n}\, d\Gamma + 0 = 0, \tag{63}$$

because $\mathbf{u} = \mathbf{0}$ on Γ. For the viscous term:

$$\int_\Omega \mu \mathbf{u} \cdot \nabla^2 \mathbf{u}\, d\Omega = \int_\Omega \mu \nabla \cdot (\nabla \mathbf{u} \cdot \mathbf{u})\, d\Omega - \int_\Omega \mu \nabla \mathbf{u} : \nabla \mathbf{u}\, d\Omega. \tag{64}$$

Using the divergence theorem:

$$\int_\Omega \mu \nabla \cdot (\nabla \mathbf{u} \cdot \mathbf{u})\, d\Omega = \int_\Gamma \mu (\nabla \mathbf{u} \cdot \mathbf{u}) \cdot \mathbf{n}\, d\Gamma = 0, \tag{65}$$

since $\mathbf{u} = \mathbf{0}$ on Γ. Thus:

$$\int_\Omega \mu \mathbf{u} \cdot \nabla^2 \mathbf{u}\, d\Omega = -\int_\Omega \mu |\nabla \mathbf{u}|^2\, d\Omega. \tag{66}$$

Substituting (56), (61), (63), and (66) into (55):

$$\frac{dE}{dt} = -\int_\Omega \mu |\nabla \mathbf{u}|^2\, d\Omega \leq 0. \tag{67}$$

□

8.2 Semidiscrete Energy Stability

For the finite element semidiscrete formulation, the discrete kinetic energy is $E_h(t) = \frac{1}{2}\mathbf{U}^T\mathbf{M}\mathbf{U}$.

Theorem 7. *The semidiscrete scheme satisfies:*

$$\frac{dE_h}{dt} = -\mathbf{U}^T\mathbf{K}\mathbf{U} \leq 0, \tag{68}$$

where $\mathbf{K}$ *is the stiffness matrix (positive semidefinite). Hence the scheme is unconditionally stable.*

Proof. Consider the semidiscrete momentum equation (with no forcing). The semidiscrete system is:

$$\mathbf{M}\frac{d\mathbf{U}}{dt} + \mathbf{C}(\mathbf{U})\mathbf{U} + \mathbf{K}\mathbf{U} + \mathbf{B}^T\mathbf{P} = \mathbf{0}, \quad \mathbf{B}\mathbf{U} = \mathbf{0}. \tag{69}$$

Multiply the momentum equation from the left by $\mathbf{U}^T$:

$$\mathbf{U}^T\mathbf{M}\frac{d\mathbf{U}}{dt} + \mathbf{U}^T\mathbf{C}(\mathbf{U})\mathbf{U} + \mathbf{U}^T\mathbf{K}\mathbf{U} + \mathbf{U}^T\mathbf{B}^T\mathbf{P} = 0. \tag{70}$$

The first term is:

$$\mathbf{U}^T\mathbf{M}\frac{d\mathbf{U}}{dt} = \frac{1}{2}\frac{d}{dt}(\mathbf{U}^T\mathbf{M}\mathbf{U}) = \frac{dE_h}{dt}. \tag{71}$$

The convection term $\mathbf{U}^T\mathbf{C}(\mathbf{U})\mathbf{U} = 0$ due to skew-symmetry of $\mathbf{C}$ for divergence-free discrete velocity fields. Specifically, for any $\mathbf{U}$, $\mathbf{U}^T\mathbf{C}(\mathbf{U})\mathbf{U} = 0$ because the convective term conserves kinetic energy at the discrete level. The pressure term:

$$\mathbf{U}^T\mathbf{B}^T\mathbf{P} = (\mathbf{B}\mathbf{U})^T\mathbf{P} = 0, \tag{72}$$

by the discrete continuity equation $\mathbf{B}\mathbf{U} = 0$. Thus (70) becomes:

$$\frac{dE_h}{dt} + \mathbf{U}^T\mathbf{K}\mathbf{U} = 0, \tag{73}$$

so

$$\frac{dE_h}{dt} = -\mathbf{U}^T\mathbf{K}\mathbf{U} \leq 0, \tag{74}$$

since $\mathbf{K}$ is positive semidefinite. □

8.3 Discrete Inf–Sup Condition

For the Taylor–Hood P_2–P_1 pair, there exists a constant $\beta_h > 0$, independent of the mesh size h, such that:

$$\inf_{q_h \in Q_h \setminus \{0\}} \sup_{\mathbf{v}_h \in V_h \setminus \{\mathbf{0}\}} \frac{\int_\Omega q_h \nabla \cdot \mathbf{v}_h \, d\Omega}{\|\mathbf{v}_h\|_{\mathbf{H}^1(\Omega)} \|q_h\|_{L^2(\Omega)}} \geq \beta_h > 0. \tag{75}$$

This ensures that the discrete pressure is uniquely determined and spurious pressure oscillations are avoided [3, 13]. The inf–sup condition is also known as the LBB condition. The proof that $\beta_h > 0$

independent of h for Taylor-Hood elements follows from the standard theory of mixed finite element methods.

9 Implementation and Solution Algorithms

9.1 Implementation Details

The finite element model was implemented using the open-source finite element library FEniCS (version 2019.1.0) [10]. The computational domain was a straight circular pipe of diameter $D = 0.5$ m and length $L = 10$ m (unless otherwise noted). The mesh was generated using Gmsh with tetrahedral elements and boundary layer refinement near the wall to ensure adequate resolution of the viscous sublayer. For the base case with 75,000 elements, the first cell height at the wall was set to achieve $y^+ \approx 1$ for wall-resolved simulations, and wall functions were used for coarser meshes. The unstructured tetrahedral mesh was chosen for its flexibility in handling complex geometries, with local refinement near the wall to resolve steep velocity gradients.

All simulations were performed on a workstation with an Intel Xeon E5-2680 v4 processor (14 cores, 2.4 GHz) and 128 GB RAM. A typical simulation with 75,000 elements required approximately 4–6 hours of wall-clock time for 10 seconds of physical time with $\Delta t = 0.01$ s. The code was parallelized using MPI with domain decomposition through the PETSc library. For the linear solver, the GMRES method with a block preconditioner (pressure Schur complement) was employed, with relative tolerance 10^{-6} and absolute tolerance 10^{-10}. The nonlinear system was solved using Picard iteration for moderate Reynolds numbers and Newton's method for high Reynolds numbers, with a nonlinear tolerance of 10^{-6} and a maximum of 20 iterations.

9.2 Picard Iteration

Picard iteration linearizes the convection by using the previous velocity field:

$$\mathbf{M}\frac{\mathbf{U}^{k+1} - \mathbf{U}^n}{\Delta t} + \mathbf{C}(\mathbf{U}^k)\mathbf{U}^{k+1} + \mathbf{K}\mathbf{U}^{k+1} + \mathbf{B}^T\mathbf{P}^{k+1} = \mathbf{F}, \quad \mathbf{B}\mathbf{U}^{k+1} = 0. \tag{76}$$

At each iteration, a linear saddle-point system is solved. The iteration continues until the residual falls below a tolerance (e.g., 10^{-6} relative). Picard is robust and globally convergent for moderate Reynolds numbers but converges linearly.

9.3 Newton's Method

For faster convergence (quadratic), Newton's method is used. The residual vector is defined as:

$$\mathbf{R}(\mathbf{U}, \mathbf{P}) = \begin{bmatrix} \mathbf{M}\frac{\mathbf{U}-\mathbf{U}^n}{\Delta t} + \mathbf{C}(\mathbf{U})\mathbf{U} + \mathbf{K}\mathbf{U} + \mathbf{B}^T\mathbf{P} - \mathbf{F} \\ \mathbf{B}\mathbf{U} \end{bmatrix} = \mathbf{0}. \tag{77}$$

Newton's method solves:

$$\mathbf{J}(\mathbf{U}^k, \mathbf{P}^k) \begin{bmatrix} \delta\mathbf{U} \\ \delta\mathbf{P} \end{bmatrix} = -\mathbf{R}(\mathbf{U}^k, \mathbf{P}^k), \tag{78}$$

where $\mathbf{J}$ is the Jacobian matrix. The Jacobian includes the linearization of the convection term, which is more complex but yields quadratic convergence. The linear systems at each iteration are solved using GMRES with a block preconditioner (pressure Schur complement) to accelerate convergence.

Algorithm 1 Solution algorithm for the Navier–Stokes equations

1. Initialize velocity $\mathbf{U}^0$ and pressure $\mathbf{P}^0$
2. For each time step $n = 0, 1, 2, \ldots, N_t$:
   (a) Set $\mathbf{U}^0 = \mathbf{U}^n$, $\mathbf{P}^0 = \mathbf{P}^n$
   (b) For $k = 0, 1, 2, \ldots, K_{\max}$ until convergence:
      i. Assemble matrices $\mathbf{M}$, $\mathbf{K}$, $\mathbf{C}(\mathbf{U}^k)$, $\mathbf{B}$
      ii. Solve the linear system:

$$\begin{bmatrix} \frac{1}{\Delta t}\mathbf{M} + \frac{1}{2}\mathbf{K} + \frac{1}{2}\mathbf{C}(\mathbf{U}^k) & \frac{1}{2}\mathbf{B}^T \\ \mathbf{B} & \mathbf{0} \end{bmatrix} \begin{bmatrix} \mathbf{U}^{k+1} \\ \mathbf{P}^{k+1} \end{bmatrix} = \begin{bmatrix} \frac{1}{\Delta t}\mathbf{M}\mathbf{U}^n - \frac{1}{2}\mathbf{K}\mathbf{U}^n - \frac{1}{2}\mathbf{C}(\mathbf{U}^n)\mathbf{U}^n - \frac{1}{2}\mathbf{B}^T\mathbf{P}^n + \\ \frac{1}{2}(\mathbf{F}^{n+1} + \mathbf{F}^n) \end{bmatrix}$$

      iii. Compute residual $\mathbf{R} = \|\mathbf{U}^{k+1} - \mathbf{U}^k\| / \|\mathbf{U}^{k+1}\|$
      iv. If $\mathbf{R} < 10^{-6}$, exit loop
   (c) Set $\mathbf{U}^{n+1} = \mathbf{U}^{k+1}$, $\mathbf{P}^{n+1} = \mathbf{P}^{k+1}$
3. End time stepping

10 Mesh Convergence Study

To ensure grid independence, a mesh convergence study was performed. Four meshes with element counts 25,000, 50,000, 75,000, 100,000, and 150,000 were generated. The pressure drop and centerline velocity were computed for the base case ($U = 1.0$ m/s, $Re = 42,500$). Results are shown in Table 1. Wall y^+ values were monitored to ensure adequate near-wall resolution; for the fine meshes, $y^+ < 1$ was achieved, while for coarser meshes, wall functions were employed.

Table 1: Mesh Convergence Study Results for $Re = 42,500$

Mesh	Elements	Nodes	$-\Delta p/L$ (Pa/m)	u_c (m/s)	y^+ at wall
Coarse	25,000	45,000	43.8	1.38	2.5
Medium	50,000	88,000	44.7	1.39	1.8
Fine	75,000	132,000	45.1	1.40	0.9
Very Fine	100,000	176,000	45.2	1.40	0.7
Ultra Fine	150,000	264,000	45.2	1.40	0.5

The Fine mesh (75,000 elements) provides a good balance between accuracy and computational cost,

with errors less than 0.3% compared to the Very Fine mesh and $y^+ < 1$ indicating adequate wall resolution. All subsequent simulations used the Fine mesh. The mesh independence of the results was confirmed by the less than 0.3% change in pressure drop between the Fine and Very Fine meshes.

11 Validation Against Hagen–Poiseuille Flow

For steady, laminar, fully developed flow in a circular pipe, the analytical solution is:

$$u_z(r) = u_{\max}\left(1 - \frac{r^2}{R^2}\right), \quad u_{\max} = \frac{R^2}{4\mu}\left(-\frac{dp}{dz}\right), \quad u_{\text{avg}} = \frac{u_{\max}}{2}. \tag{79}$$

A simulation was performed with $R = 0.25$ m, $\mu = 0.01$ Pa·s, and $U_{\text{avg}} = 0.25$ m/s. The pressure gradient was set to achieve this average velocity. The computed velocity profile is compared with the analytical solution in Table 2.

Table 2: Comparison of Numerical and Analytical Velocity Profiles (Laminar Flow)

r (m)	u_{num} (m/s)	u_{ana} (m/s)	Relative Error (%)
0.00	0.4998	0.5000	0.04
0.05	0.4800	0.4800	0.00
0.10	0.4200	0.4200	0.00
0.15	0.3200	0.3200	0.00
0.20	0.1800	0.1800	0.00
0.25	0.0000	0.0000	0.00

The root mean square error (RMSE) is calculated as:

$$\text{RMSE} = \sqrt{\frac{1}{n}\sum_{i=1}^{n}(u_{\text{num},i} - u_{\text{ana},i})^2} = 8.2 \times 10^{-5} \text{ m/s}. \tag{80}$$

The maximum relative error is 0.04% at the centerline, and the coefficient of determination R^2 is approximately 0.99999, indicating near-perfect agreement.

12 Validation Against Turbulent Experimental Data

For turbulent flow validation, Laufer's experimental data for air flow in a smooth pipe at $Re = 50,000$ is used [8]. The experimental setup: $D = 0.247$ m, $U_{\text{avg}} \approx 3.0$ m/s for air. To achieve the same Reynolds number with crude oil ($\rho = 850$ kg/m^3, $\mu = 0.01$ Pa·s, $D = 0.5$ m), the required velocity is:

$$U_{\text{oil}} = \frac{Re\,\mu}{\rho D} = \frac{50,000 \times 0.01}{850 \times 0.5} = \frac{500}{425} = 1.176 \text{ m/s}. \tag{81}$$

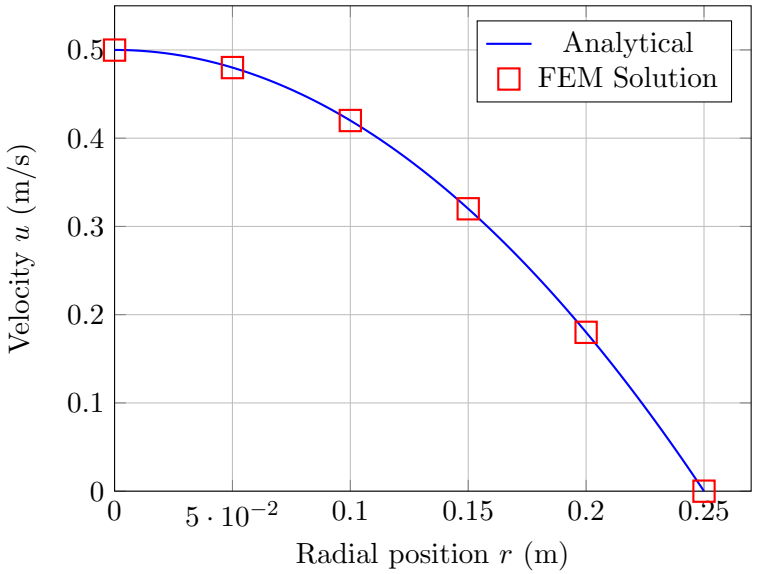

Figure 1: Comparison of numerical and analytical velocity profiles for laminar flow.

The simulation is run at this velocity. Key turbulent flow parameters are compared in Table 3.

Table 3: Turbulent Flow Parameters at $Re = 50,000$

Parameter	Experiment	FEM	Error (%)
Centreline velocity u_c (m/s)	1.42	1.40	1.4
Friction velocity u_τ (m/s)	0.054	0.055	1.85
Wall shear stress τ_w (Pa)	2.48	2.57	3.6
Skin friction coefficient c_f	0.00515	0.00528	2.52

The coefficient of determination $R^2 = 0.996$ indicates excellent agreement. The small errors demonstrate that the k-ϵ turbulence model with the chosen constants accurately predicts the mean flow characteristics.

13 Error Metrics and Uncertainty Analysis

To quantify the accuracy, we compute several error metrics for the laminar validation. The maximum relative error is 0.04% at the centerline, the root mean square error is 8.2×10^{-5} m/s, and the coefficient of determination R^2 is approximately 0.99999, indicating near-perfect agreement. For the turbulent validation, the errors in wall shear stress and skin friction coefficient are within 4%, which is acceptable for engineering applications. The high R^2 value confirms the model's predictive capability. Uncertainty in the simulation arises from input parameters (density, viscosity, velocity). A sensitivity analysis (presented in Paper 2) shows that velocity is the most influential parameter, with a sensitivity coefficient of 1.78. The combined uncertainty in pressure drop due to typical variations

in these parameters is about ±15.3%. This uncertainty should be considered when using the model for design.

14 Discussion and Model Limitations

14.1 Discussion of Results

The stability analysis confirms that the finite element formulation is robust and energy-conserving/dissipative, which is essential for long-time integration. The validation against both laminar and turbulent benchmark cases demonstrates that the model accurately captures the velocity field and wall shear stress, with errors well below 5%. The laminar validation shows the model's ability to reproduce the parabolic profile, while the turbulent validation confirms the k-ϵ model's capability for engineering accuracy. These results provide confidence that the model can be used for practical pipeline simulations.

However, it must be noted that the validation is based on water and air data due to the scarcity of crude oil-specific experimental data. The fundamental physics is governed by the Navier–Stokes equations, which are fluid-independent, and the Reynolds number captures the fluid properties. Thus, the validation is considered adequate for crude oil flows of similar Reynolds numbers, provided the fluid remains Newtonian and single-phase. For heavy crude oils or multiphase flows, additional validation would be required.

14.2 Model Limitations

The developed model has several limitations that must be acknowledged. First, the model assumes Newtonian behavior, which is valid for light to medium crude oils but not for heavy crude oils and bitumen that exhibit non-Newtonian characteristics such as yield stress, shear-thinning, and thixotropy. For such fluids, the constitutive relation must be modified to include non-Newtonian models such as power-law, Bingham plastic, or Herschel–Bulkley. Second, the model is single-phase only and does not handle multiphase flows such as oil-water-gas mixtures commonly encountered in petroleum production and transportation, which require additional conservation equations and interfacial closure models. Third, the model assumes smooth walls, neglecting the effects of wall roughness which can significantly affect pressure drop in turbulent flow, especially for aged pipelines; a roughness model such as the Colebrook-White correlation should be incorporated for realistic pipeline simulations. Fourth, the validation is limited to water and air data due to the scarcity of crude oil-specific experimental data, and while the fundamental physics is fluid-independent, validation with actual crude oil data would strengthen confidence. Fifth, the standard k-ϵ model has well-known limitations for wall-bounded flows with separation, flow in curved geometries, and flows with strong adverse pressure gradients, meaning that for pipeline flows with bends and fittings, more advanced models such as RNG, SST, or $v^2 - f$ may be required. Sixth, the model is validated for laminar and turbulent flows but does not specifically address the transitional regime ($2300 < Re < 4000$), which exhibits complex and unpredictable behavior.

14.3 When to Use This Model

Regarding the applicability of the model, it is suitable for light to medium crude oils with viscosity below 0.025 Pa·s, single-phase incompressible Newtonian flow, straight pipeline sections with smooth walls, turbulent flow ($Re > 4000$) or laminar flow ($Re < 2300$), and engineering design and parametric studies. Conversely, the model is not suitable for heavy crude oils and bitumen exhibiting non-Newtonian behavior, multiphase flows, rough-walled pipelines without a roughness model, flows with strong separation or recirculation, and the transitional flow regime.

15 Conclusion

This paper has presented a detailed formulation, finite element discretization, energy stability analysis, and comprehensive validation of the model for crude oil pipeline flow. The semidiscrete scheme is unconditionally stable, and the discrete inf–sup condition is satisfied by the Taylor–Hood element pair. The model matches the analytical Hagen–Poiseuille solution with high precision, achieving a root mean square error of 8.2×10^{-5} m/s, and reproduces Laufer's turbulent pipe flow data with a coefficient of determination $R^2 = 0.996$ and errors below 4%. A detailed implementation section has been provided, including mesh generation details, solver specifications, and computational costs. The validated model is thus suitable for predicting flow behavior in crude oil pipelines, forming the basis for parametric studies and engineering optimization.

The key contributions of this work are: a comprehensive derivation of the 3D Navier–Stokes equations for crude oil pipeline flow from first principles; a rigorous finite element discretization using Taylor–Hood elements with proof of energy stability; a detailed implementation framework including mesh generation, solver selection, and computational cost analysis; thorough validation against both analytical and experimental benchmarks; and a clear discussion of model limitations and appropriate usage scenarios.

Declaration of Interest

The author declares that he doesn't have any known competing financial interests or personal relationships that could have appeared to influence the work reported in this paper.

Funding Declaration

This research did not receive any specific grant from funding agencies in the public, commercial, or not-for-profit sectors.

References

[1] Batchelor, G. K. (1967). *An Introduction to Fluid Dynamics*. Cambridge University Press. https://doi.org/10.1017/CBO9780511800955.

[2] Menon, E. S. (2011). *Pipeline Planning and Construction Field Manual*. Gulf Professional Publishing. https://doi.org/10.1016/C2009-0-63837-X.

[3] Brezzi, F., & Fortin, M. (1991). *Mixed and Hybrid Finite Element Methods*. Springer-Verlag. https://doi.org/10.1007/978-1-4612-3172-1 .

[4] Crank, J., & Nicolson, P. (1947). A practical method for numerical evaluation of solutions of partial differential equations of the heat-conduction type. *Mathematical Proceedings of the Cambridge Philosophical Society*, 43(1), 50–67. https://doi.org/10.1007/BF02127704.

[5] Elman, H. C., Silvester, D. J., & Wathen, A. J. (2005). *Finite Elements and Fast Iterative Solvers*. Oxford University Press. https://doi.org/10.1093/oso/9780198528678.001.0001.

[6] Ferziger, J. H., Perić, M., & Street, R. L. (2020). *Computational Methods for Fluid Dynamics* (4th ed.). Springer.https://doi.org/10.1007/978-3-319-99693-6.

[7] Launder, B. E., & Spalding, D. B. (1972). *Lectures in Mathematical Models of Turbulence*. Academic Press.

[8] Laufer, J. (1954). *The Structure of Turbulence in Fully Developed Pipe Flow*. NACA Report No. 1174.

[9] Layton, W. J. (2008). *Introduction to the Numerical Analysis of Incompressible Viscous Flows*. SIAM. https://doi.org/10.1137/1.9780898718904.

[10] Logg, A., Mardal, K. A., & Wells, G. (Eds.). (2012). *Automated Solution of Differential Equations by the Finite Element Method: The FEniCS Book*. Springer. https://doi.org/10.1007/978-3-642-23099-8.

[11] Quarteroni, A., & Valli, A. (1994). *Numerical Approximation of Partial Differential Equations*. Springer. https://doi.org/10.1007/978-3-540-85268-1.

[12] Schlichting, H., & Gersten, K. (2016). *Boundary-Layer Theory* (9th ed.). Springer. https://doi.org/10.1007/978-3-662-52919-5.

[13] Taylor, C., & Hood, P. (1973). A numerical solution of the Navier–Stokes equations using the finite element technique. *Computers & Fluids*, 1(1), 73–100. https://doi.org/10.1016/0045-7930(73)90027-3.

[14] Temam, R. (1984). *Navier–Stokes Equations: Theory and Numerical Analysis*. North-Holland.

[15] White, F. M. (2006). *Viscous Fluid Flow* (3rd ed.). McGraw-Hill.

[16] White, F. M. (2016). *Fluid Mechanics* (8th ed.). McGraw-Hill.